IEEE Photonics Journal
An IEEE Photonics Society Publication

Open Access

A 1Mbps Real-Time NLOS UV Scattering Communication System With Receiver Diversity Over 1km

Volume 10, Number 2, April 2018

Guanchu Wang
Kun Wang
Chen Gong
Difan Zou
Zhimeng Jiang
Zhengyuan Xu

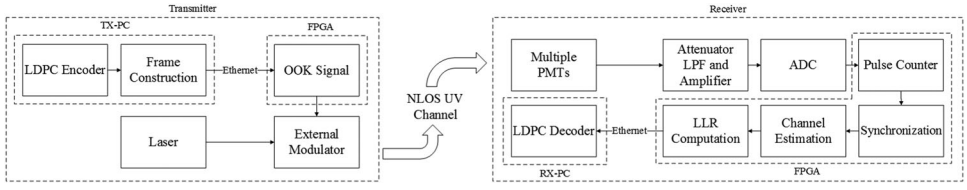

DOI: 10.1109/JPHOT.2018.2822690
1943-0655

IEEE photonics SOCIETY

IEEE

A 1Mbps Real-Time NLOS UV Scattering Communication System With Receiver Diversity Over 1km

Guanchu Wang,[1] Kun Wang,[1] Chen Gong,[1] Difan Zou,[1] Zhimeng Jiang,[1] and Zhengyuan Xu [1,2]

[1]Key Laboratory of Wireless-Optical Communications, Chinese Academy of Sciences, School of Information Science and Technology, University of Science and Technology of China, Hefei 230000, China
[2]Shenzhen Graduate School, Tsinghua University, Shenzhen 518055, China

DOI:10.1109/JPHOT.2018.2822690

Manuscript received March 11, 2018; revised March 28, 2018; accepted March 29, 2018. Date of publication April 6, 2018; date of current version April 12, 2018. This work was supported in part by the Key Program of National Natural Science Foundation of China under Grant 61631018, and in part by the Key Research Program of Frontier Sciences of CAS under Grant QYZDY-SSW-JSC003. Corresponding author: Chen Gong (e-mail: cgong821@ustc.edu.cn).

Abstract: In the nonline of sight (NLOS) ultraviolet (UV) scattering communication, the received signals exhibit the characteristics of discrete photoelectrons due to the extremely large path loss. We design and demonstrate an NLOS UV scattering communication system in this paper, where the receiver-side signal detection is designed based on a discrete-time Poisson channel model. In our system, a laser and multiple photomultiplier tubes are employed as the optical transmitter and detector, respectively. Furthermore, we design algorithms for pulse-counting, synchronization, channel estimation, and LLR computation for hardware realization in field-programmable gate array board. Simulation results are provided to evaluate the proposed system design and specify the system key parameters for real-time implementation. We perform field tests for real-time communication with the transmission range over 1 km, where the system throughput reaches 1 Mbps.

Index Terms: Non-line of sight (NLOS), ultraviolet (UV) scattering communication, discrete-time Poisson channel, receiver diversity.

1. Introduction

1.1 Background and Organization

Non-Line of sight (NLOS) scattering communication can maintain certain transmission rate for optical wireless communication (OWC) while not requiring perfect alignment of the transmitter and receiver [1]–[3]. Prospective application of NLOS scattering communication includes the scenarios where radio-silence is required and the transmitter-receiver alignment is hard to guarantee due to obstacles or mobility. Existing works based on NLOS visible light communication (VLC) have been reported in [4]–[6]. However, VLC may suffer strong solar interfernece especially during daytime, while the background radiation of ultraviolet (UV) communication within spectrum between 200 nm and 280 nm is negligible since most solar radiation in such spectrum is absorbed by the atmosphere [2]. Hence the NLOS UV scattering communication serves as a good candidate for outdoor OWC in the cases of non-perfect transmitter-receiver alignment and strong solar background radiation.

NLOS UV scattering communication has been extensively investigated from both theoretic and experimental perspectives recently, which can be characterized by Poisson channel. The capacities of continuous-time and discrete-time Poisson channel have been studied in [7], [8] and [9], [10], respectively. Moreover, the capacities of MISO and MIMO communication have been investigated in [11] and [12], respectively. Regarding the channel characterization, the channel link gain and impulse response model have been extensively investigated in [13]–[18]. The receiver-side signal characterization and performance analysis has been studied in [19]. The generalized maximum-likelihood sequence detection has been discussed in [20], and the signal detection with receiver diversity has been investigated in [21], [22]. Besides the theoretical investigation, experiment works on the NLOS UV scattering channel characterization include the turbulence channel investigation [23], [24], the UV photon-counting based detection [25], and long-distance channel characterization [26].

In this work, we realize the real-time communication over 1 km NLOS transmission link with 1 Mbps throughput. We still employ an UV laser as the transmitter, with an external-modulator for on-off keying (OOK) modulation. Receiver diversity is adopted with equal gain combining since the signal intensities at different detectors are approximately the same. We design and realize signal processing algorithms based on the discrete-time Poisson channel model. Computer-based simulations are conducted to evaluate the performance of the designed communication system. Furthermore, we realize a real-time point-to-point SIMO UV communication system consisting of multiple photomultiplier tubes (PMTs) with optical devices and amplifying circuits, field-programmable gate array (FPGA) boards for implementation of digital signal processing, and computers for real-time encoding and decoding of channel codes in software. We complete a real-time communication experiment with the transmission distance over 1 km and the resulting throughput can reach 1 Mbps.

This remainder is organized as follows. In Section 1.2 we summarize the related works on UV scattering communication. In Section 2, we provide the channel model and block diagrams of the proposed communication system. In Section 3, we address the signal processing at the receiver side. Simulation and real-time experimental measurement results are shown in Section 4. Finally, we conclude this paper in Section 5.

1.2 Related Works on the Realization of UV Scattering Communication

For NLOS UV scattering communication, the transmission distance and data rate are limited by the receiver-side sign-to-noise ratio (SNR), which depends on the channel path loss and atmospheric turbulence-induced fading. Research works on the experimental communication system realization have been conducted with several representative endeavors. Experimental communication systems with transmission data rate of 2 kbps over 100 m distance have been reported in [27]. Real-time systems with nearly 2.4 kbps air-face data rate over 90 m LOS transmission links, experiment with 500 kbps air-face data rate over 50 m NLOS transmission links based on RS/LDPC codes and semi-real-time system with nearly 80 kbps air-face data rate over 30 m NLOS transmission links have been accomplished in [28]–[30], respectively. Based on simulation results with measured parameters, the link budget analysis for nearly 1 Mbps throughput over 80 m NLOS transmission is performed in [31]. Furthermore, demonstration of 400 kbps throughput over 500 m transmission link based on concatenated codes has been realized in [32]. We summarize the above related works in Table 1, where the our current work shows improvements in the aspects of transmission distance or data rate or both.

2. Signal Characterization and System Block Diagram

2.1 Discrete-time Poisson Channel with Receiver Diversity

Consider the NLOS UV scattering communication system with receiver diversity. We employ a UV laser with constant power $\widetilde{P}_t$ at the transmitter side. An acousto-optic (AO) modulator is used for the on-off keying (OOK) modulation, which changes the direction of the UV light beam for symbol

TABLE 1
Comparison Between Our Work and Related Works

Reference	Distance	Data rate	Link	Transmission
[27]	100m	2kbps	LOS	Non-real time
[28]	90m	2.4kbps	LOS	Real-time
[29]	50m	500kbps	NLOS	Non-Real time
[30]	30m	80kbps	NLOS	Semi-real time
[31]	80m	1Mbps	NLOS	Simulation
[32]	500m	400kbps	NLOS	Real-time
Our work	1km	1Mbps	NLOS	Real-time

s_k, such that for $s_k = 0$ the light can be blocked at the transmitter side while for $s_k = 1$ the light can be emitted. At the receiver side, multiple detectors are employed to increase the received signal intensity. Due to the extremely large path loss of the NLOS scattering communication, the detected signal can be characterized by discrete photoelectrons whose number satisfies a Poisson distribution. We assume that given the transmitted symbols and the link gains of the receivers, the numbers of photoelectrons for different detectors are independent of each other due to independent photon reception and photoelectric conversion of different detectors.

Assume that K detectors are employed at the receiver side. Let N_k denote the number of received photoelectrons from detector k, which satisfies the following Poisson distribution

$$\begin{aligned}\mathbb{P}(N_k = n|s = 1) &= \frac{(\lambda_{s,k} + \lambda_{b,k})^n}{n!} e^{-(\lambda_{s,k}+\lambda_{b,k})},\\ \mathbb{P}(N_k = n|s = 0) &= \frac{\lambda_{b,k}^n}{n!} e^{-\lambda_{b,k}},\end{aligned} \tag{1}$$

where $\lambda_{s,k}$ and $\lambda_{b,k}$ denote the mean numbers of detected photoelectrons at detector k for the signal and background radiation components, respectively. For the transmission symbol rate R_s under OOK modulation, we have that

$$\lambda_{s,k} = \frac{\eta_k \widetilde{P}_t}{\xi_k h \nu R_s}, \tag{2}$$

where η_k, h, ν and ξ_k denote the quantum efficiency of detector k including optical filter and photon-detector, Planck's constant, the frequency of the optical signal and the path loss from the transmitter to detector k, respectively.

2.2 Communication System Block Diagram

At the transmitter side, the information bits are randomly generated and encoded in the transmitter-side personal computer (TX-PC). The encoded blocks are divided into transmission frames and sent from the TX-PC to the FPGA board via ethernet cable. On the FPGA board, the synchronization and pilot sequences are added at the head of each frame and certain protection intervals are added between consecutive frames. The frames with protection intervals are exported to the RF driver via the pin of FPGA board, which drive the AO modulator of the UV laser.

At the receiver side, PMTs are employed as the photon-detector, which can convert the received photoelectrons to analog pulses such that photon counting can be realized via pulse counting. A HAMAMATSU PMT (R7154 module) detector is sealed into a shielding box, which is integrated with a UV optical filter that passes the light signal of wavelength around 266 nm and blocks the solar background radiation on other wavelengths. To enable effective pulse counting process, attenuators, low-pass filters and amplifiers are adopted. The pulses are firstly attenuated by the electrical attenuator such that it falls into the input range of the amplifier and then amplified. The amplified pulses pass through the low-pass filter such that the pulse width can be increased and the rising edge detection for pulse counting can be performed more accurately. Analog-to-digital

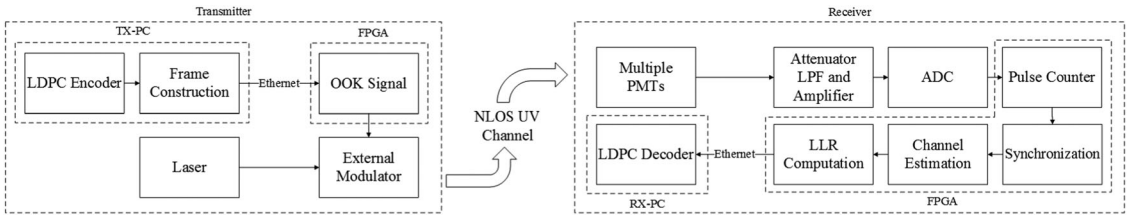

Fig. 1. The block diagram of NLOS UV scattering communication system.

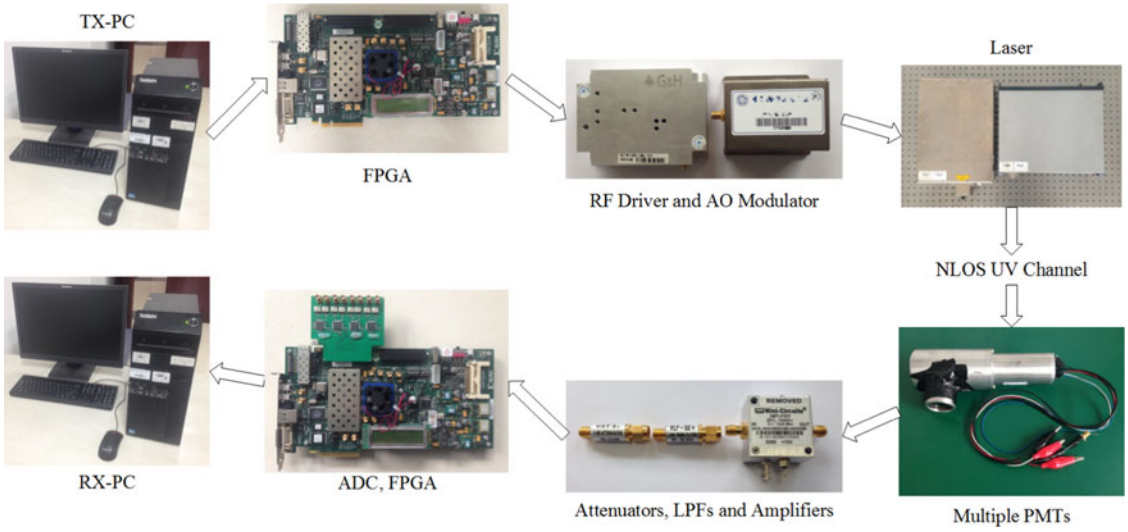

Fig. 2. The hardware realization blocks for the NLOS UV scattering communication system.

converters (ADCs) are employed such that the rising edge detection can be performed in the digital domain. The digital processing of synchronization, channel estimation and symbol detection are performed sequentially based on discrete-time Poisson channel characterization in the FPGA board. To achieve the processing for receiver diversity, a Xilinx Virtex-6 ML605 board is adopted to support multiple ADCs. The soft information of received signal detection is packed at the FPGA board and sent to the receiver-side personal computer (RX-PC) through the ethernet cable, which is employed for decoding at the receiver side. The block diagram and experimental system of the entire NLOS UV scattering communication link are shown in Figs. 1 and 2, respectively.

3. Digital Signal Processing in Hardware Realization

We outline the digital signal processing in FPGA hardware realization, including the pulse counting with receiver diversity combining, the counting-based synchronization, the counting-based channel estimation and LLR computation, and the LDPC construction and decoding.

3.1 Pulse-count and Receiver Diversity Combining

Based on the output waveform of the AD-convertor for each PMT, the pulse counting can be realized according to the rising-edge detection with a voltage threshold V_{thd}. A pulse can be recorded if the previous sample voltage is lower than V_{thd} and the current sample is higher than V_{thd}.

Note that since the K PMTs are placed close to each other, the received signal intensities are virtually the same. Then the maximum-likelihood detection among the K detectors can be approximated by equal gain combining, which is adopted for K PMTs in this work.

Let N_k denote the number of pulses of PMT k in a symbol duration. For the equal gain combining, letting $N = \sum_{k=1}^{K} N_k$, with the signal component intensity $\lambda_s \triangleq \sum_{k=1}^{K} \lambda_{s,k}$ and noise component intensity $\lambda_b \triangleq \sum_{k=1}^{K} \lambda_{b,k}$, we have that N satisfies a Poisson distribution with mean $(\lambda_s + \lambda_b)$ for OOK symbol on and the mean λ_b for OOK symbol off. Due to the Poisson channel characteristics, such signal combination can significantly improve the communication system performance.

3.2 Counting-based Synchronization

Note that the pulse-counting has been investigated in [33]. We employ pulse-counting-based digital signal processing for synchronization. Since the starting time of a frame is difficult to detect, in this work the received signal is considered to be divided into chips with duration $T_c = \frac{T_s}{M}$, where T_s denotes the duration of one symbol. For certain chip index t, the numbers of pulses in the past $L\,M$ consecutive chips are reserved in an $L \times M$ matrix $\boldsymbol{C}_t$, where each element denotes the number of pulses in chip $t-(i-1)M-j+1$ for $1 \le i \le L$ and $1 \le j \le M$. Let $\boldsymbol{s}$ denote the chip-level synchronization sequence containing the $L\,M$ consecutive chips corresponding to the L binary symbols. The synchronization is formulated by the following maximum auto-correlation problem,

$$\hat{t} = \arg\max_{t} \left\{ (2\boldsymbol{s}^T - \mathbf{1}_L^T)\boldsymbol{C}_t \mathbf{1}_M \right\}, \tag{3}$$

where $\mathbf{1}_L^T$ and $\mathbf{1}_M$ are all-one L-dimensional row and M-dimensional column vector, respectively; and $\hat{t}$ denotes the estimated ending index of the synchronization sequence.

The synchronization based on (3) requires finding the optimal $\hat{t}$ with the maximum correlation peak among all possible positions, which leads to a large delay in hardware realization. To reduce the delay, we adopt reduced-complexity synchronization based on shortening the search window. Let C_{thd} denote a threshold for activating the peak value searching, and W denote the width of the searching window, which are pre-determined via training from existing experimental results. The search on the maximum correlation peak is activated in the interval $[\tilde{t},\ \tilde{t} + WT_c)$, once $\boldsymbol{s}^T \boldsymbol{C}_{\tilde{t}} \mathbf{1}_M > C_{thd}$. The performance of proposed algorithm depends on the preset values of C_{thd} and W, where a time delay WT_c is brought by the proposed peak value searching. Note that a long synchronization searching window length may incur a large delay while too short searching window length may incur synchronization error. On the other hand, miss synchronization may happen for a large searching threshold and wrong synchronization may happen for a small searching threshold. Both searching window length and searching threshold need to be optimized. In this work, we perform extensive simulations on different signal and background intensities, and select the searching window length and threshold with negligible synchronization error according to the simulation results.

3.3 Channel Estimation and LLR Coumputation

The synchronization sequence is also adopted for channel parameter estimation. Letting $\boldsymbol{C}_s$ denote the number of pulses in the pilot symbols corresponding to synchronization sequence $\boldsymbol{s}$, we have $\boldsymbol{C}_s = \boldsymbol{C}_{\hat{t}-WT_c}$ due to the synchronization delay, where the number of pulses for each symbol can be obtained via merging those of consecutive M chips. Hence the mean of signal component λ_s and background radiation λ_b for each symbol can be estimated by the following unbiased estimation,

$$\begin{aligned} \widehat{\lambda}_b + \widehat{\lambda}_s &= \frac{\boldsymbol{s}^T \boldsymbol{C}_s \mathbf{1}_M}{\boldsymbol{s}^T \mathbf{1}_L}, \\ \widehat{\lambda}_b &= \frac{\bar{\boldsymbol{s}}^T \boldsymbol{C}_s \mathbf{1}_M}{\bar{\boldsymbol{s}}^T \mathbf{1}_L}, \end{aligned} \tag{4}$$

where $\bar{\boldsymbol{s}} = \mathbf{1}_L - \boldsymbol{s}$. Since N has been denoted as the number of pulses in one symbol, according to (1), the log-likelihood ratio (LLR), denoted as $\mathcal{L}(N)$, is given by

$$\mathcal{L}(N) = N \log\left(\frac{\widehat{\lambda}_s + \widehat{\lambda}_b}{\widehat{\lambda}_b}\right) - \widehat{\lambda}_s \sim N - \frac{\widehat{\lambda}_s}{\log\left(\frac{\widehat{\lambda}_s + \widehat{\lambda}_b}{\widehat{\lambda}_b}\right)}. \tag{5}$$

The hardware realization of channel estimation and LLR-computation is based on (4) and (5), respectively. Since the division operation is difficult to realize in a real-time high-speed manner, to reduce the computational complexity of channel estimation, the quantized results of division $\theta_i^s = (p_s i)^{-1}$ and $\theta_i^b = (p_b i)^{-1}$ for $1 \le i \le L$ are computed in an offline manner and stored in a table, where p_s and p_b are the preset precision on the estimation of λ_s and λ_b, respectively. The estimation for channel parameters is given by $\widehat{\lambda}_s = \theta^s_{\bar{\boldsymbol{s}}^T \mathbf{1}_L} \boldsymbol{s}^T \boldsymbol{C}_s \mathbf{1}_M$ and $\widehat{\lambda}_b = \theta^b_{\bar{\boldsymbol{s}}^T \mathbf{1}_L} \bar{\boldsymbol{s}}^T \boldsymbol{C}_s \mathbf{1}_M$, respectively.

For the low-complexity realization of LLR-computation, let $\phi_{i,j} = \lceil \frac{p_s j}{\log(\frac{p_s l + p_b l}{p_b l})} \rceil$, for $1 \le i \le \Lambda_s$ and $1 \le j \le \Lambda_b$, where Λ_s and Λ_b denote the preset maximum estimation value of λ_s and λ_b, respectively. The values of $\phi_{i,j}$ are computed offline and stored in a table. We then compute LLR via $\mathcal{L}(N) = N - \phi_{\lfloor \widehat{\lambda}_s \rfloor, \lfloor \widehat{\lambda}_b \rfloor}$ and store the results into a buffer. Once having collected the LLRs corresponding to one LDPC coded block, the messages are packed and sent to the RX-PC for LDPC decoding via the ethernet cable from the FPGA board.

$$\boldsymbol{H}_1 = \begin{bmatrix} \boldsymbol{I}_{p(0)} & \boldsymbol{I}_{p(0)} & \cdots & \boldsymbol{I}_{p(0)} \\ \boldsymbol{I}_{p(0)} & \boldsymbol{I}_{p(p_{1,1})} & \cdots & \boldsymbol{I}_{p(p_{1,D-1})} \\ \vdots & \vdots & \ddots & \vdots \\ \boldsymbol{I}_{p(0)} & \boldsymbol{I}_{p(p_{J-1,1})} & \cdots & \boldsymbol{I}_{p(p_{J-1,D-1})} \end{bmatrix} \tag{6}$$

3.4 LDPC Code Construction and Decoding

A (n_c, k_c) irregular LDPC code is employed for error correction, where n_c and k_c denote the number of coded and information symbols, respectively. We consider the construction of parity-check matrix proposed in [34]. The proposed construction of the parity check matrix $\boldsymbol{H}_{(n_c-k_c)\times n_c} = [\boldsymbol{H}_1, \boldsymbol{H}_2]$, where $\boldsymbol{H}_1$ is a regular block-wise Quasi-Cyclic (QC) low-density circular matrix [35]. A (J, D)-regular QC parity-check matrix $\boldsymbol{H}_1$ is specified in (6), where $\boldsymbol{I}_{p(p_{j,l})}$ represents the circulant permutation matrix with element one at column $[(r + p_{j,l}) \mod p]$ in row r, for $1 \le r \le p-1$, $1 \le j \le J-1$ and $1 \le l \le D-1$; and $\boldsymbol{I}_{p(0)}$ denotes a $p \times p$ identity matrix. For the girth larger than or equal to 6, we set $p_{j,l} = [(q_1^j - 1)(q_2^l - 1) \mod p]$ for $1 \le j \le J-1$ and $1 \le l \le D-1$, where p is a prime number and q_1 and q_2 are two nonzero distinct elements of $\mathbf{GF}(p)$. Moreover, $\boldsymbol{H}_2$ is a $(n_c - k_c) \times (n_c - k_c)$ square sawtooth matrix given by

$$\boldsymbol{H}_2 = \begin{bmatrix} 1 & & & & & & \\ 1 & 1 & & & & & \\ & 1 & 1 & & & & \\ & & & \cdots & & & \\ & & & & 1 & 1 & \\ & & & & & 1 & 1 \end{bmatrix}. \tag{7}$$

The systematic generator matrix $\boldsymbol{G}_{k_c \times n_c}$ corresponding to above parity check matrix $\boldsymbol{H}$ is given by $\boldsymbol{G}_{k_c \times n_c} = [\boldsymbol{I}, \boldsymbol{H}_1^T \boldsymbol{H}_2^{-T}]$, where $\boldsymbol{H}_2^{-T}$ is the binary transposed inverse of $\boldsymbol{H}_2$ given by

$$\boldsymbol{H}_2^{-T} = \begin{bmatrix} 1 & 1 & \cdots & \cdots & 1 \\ & 1 & \cdots & \cdots & 1 \\ & & & \cdots & \\ & & & 1 & 1 \\ & & & & 1 \end{bmatrix}. \tag{8}$$

We adopt the reduced-complexity message passing algorithm (MPA) for the LDPC decoding proposed in [36]. For the Tanner graph corresponding to the parity-check matrix $\boldsymbol{H}$, let $\mathcal{M}(n)$ and $\mathcal{N}(m)$ denote the set of check nodes linked to the nth variable node and the set of variable nodes

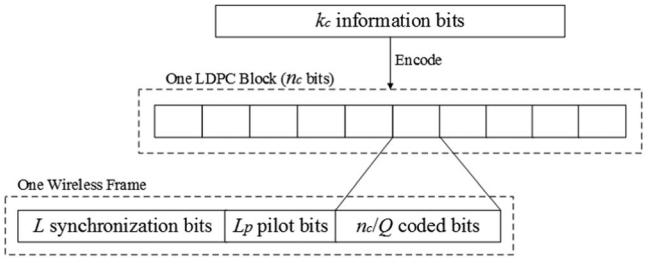

Fig. 3. The structure of a transmission frame.

connected to the mth check node. Let $L_{m\to n}(N_n)$ and $Z_{n\to m}(N_n)$ denote the message passed from the mth check node to the nth variable node and from the latter to the former, respectively.

The updating of passing message for the MPA is shown as follows. Initialize $L_{m\to n}(N_n) = 0$ and $Z_{n\to m}(N_n) = \mathcal{L}(N_n)$. The external message update at the nth check node for $n \in \mathcal{N}(m)$ is given in the following equation

$$L_{m\to n}(N_n) = \left(\prod_{n' \in \mathcal{N}(m)\backslash n} \operatorname{sgn}\left(Z_{n'\to m}(N_{n'})\right) \right) \times \frac{\min_{n' \in \mathcal{N}(m)\backslash n} |Z_{n'\to m}(N_{n'})|}{\alpha}, \tag{9}$$

where α is a normalization constant larger than one. The external message update at the mth variable node for $m \in \mathcal{M}(n)$ is given by

$$Z_{n\to m}(N_n) = \mathcal{L}(N_n) + \sum_{m' \in \mathcal{M}(n)\backslash m} L_{m'\to n}(N_n). \tag{10}$$

The decision for each symbol is based on the following equation,

$$Z_n(N_n) = \mathcal{L}(N_n) + \sum_{m \in \mathcal{M}(n)} L_{m\to n}(N_n). \tag{11}$$

The detection result $\hat{\boldsymbol{s}} \triangleq [\hat{s}_1, \hat{s}_2, \ldots, \hat{s}_{n_c}]^T$, where $\hat{s}_n = \operatorname{sgn}\left[Z_n(N_n)\right]$ for $1 \le n \le n_c$. The symbol detection is performed in each iteration, and the MPA terminates if the parity check relation is satisfied, i.e., $\boldsymbol{H}\hat{\boldsymbol{s}} = \boldsymbol{0}$. The decoding failure is recorded if the parity check relation has not been satisfied within a preset threshold of iteration times, which is typically set to be 10 or 20 in practical implementation.

Since the LDPC block length typically reaches several thousands to ten thousands, each block needs to be divided into Q segments for transmission. Synchronization and indication sequences are then added in front of each segment, where the indication sequence stores the block location of each frame in the LDPC block. Each frame contains $(\frac{n_c}{Q} + L + L_p)$ bits, where L and L_p are the lengths of synchronization sequence and indication sequence, respectively. The structure of a frame is shown in Fig. 3.

4. System Design with Simulation and Experimental Results

4.1 System Specification with Simulation Results

We specify the NLOS UV communication system under consideration. Let the number of detectors $K = 3$, the transmission symbol rate of OOK modulation $R_b = 2$ Mbps, and the number of chips within a symbol duration $M = 10$. Note that the solar background radiation is approximately 1×10^4 to 5×10^4 counts per second at the wavelength 266 nm. Due to the inter-symbol interference from the low-pass properties of the AO modulator, around half chip of pulses for OOK symbol off is affected by the previous symbol on, which implies that the background radiation intensity can increase via an amount $\frac{\lambda_s}{2M}$ if the inter-symbol interference is not taken into consideration. Hence we adopt certain margin for the background radiation intensity within each symbol duration, and set $\lambda_b \in \{0.1, 0.2, 0.3, 0.4, 0.5\}$. For rate-0.6 (12630, 7578) and rate-0.8 (12630, 10104) LDPC codes,

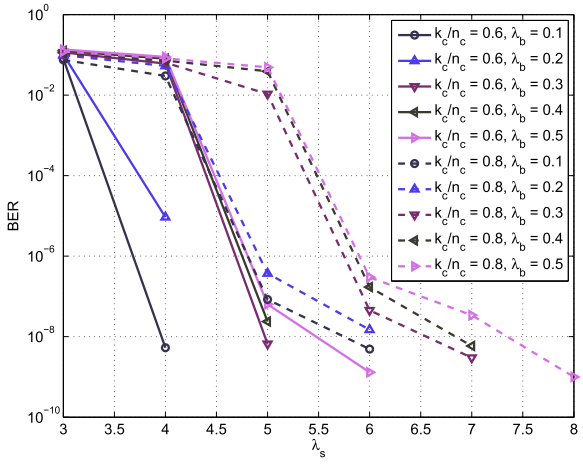

Fig. 4. The BER of LDPC code on Poisson channel for different code rates.

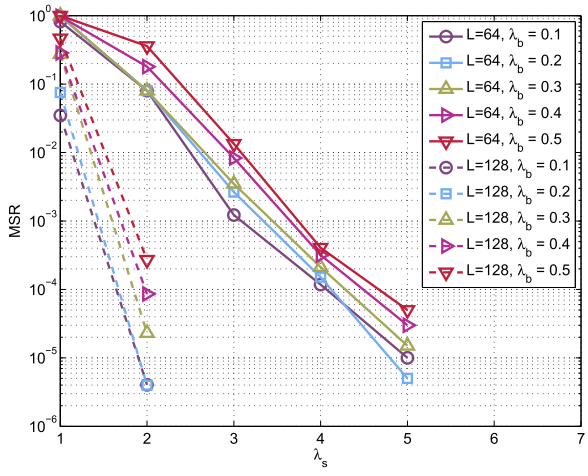

Fig. 5. The miss synchronization rata versus λ_s for different λ_b.

we show the BER versus λ_s in Fig. 4; and for the length of synchronization sequence $L = 64$ and $L = 128$, we plot the miss synchronization rate (MSR) against λ_s in Figure 5. It is observed that for rate-0.6 code, the BER can drop below 10^{-6} when $\lambda_s \geq 5.0$, where $L = 64$ suffices to suppress the MSR below 10^{-4}.

Based on above simulation results, we adopt the length of synchronization sequence $L = 64$, and the LDPC code with parameters $J = 12$, $D = 18$, $p = 421$, $k_c = 7578$, $n_c = 12630$ and code rate $k_c/n_c = 0.6$. More concrete realization parameters include: the precision of channel estimation $p_s = 0.5$, $p_b = 0.01$, the segment number $Q = 10$ and the pilot length $L_p = 17$. For such coding scheme, the simulation results for the frame error rate (FER) is shown in Figure 6.

4.2 Lab Test on the Communication System Performance

We conduct real-time lab test on the system performance before outdoor field test, with the designed system parameters from the simulation results and the devices specified in Table 2. Note that there is a slight offset between the UV laser wavelength and the optical filter peak wavelength, due to the physical constraints on the UV optical filter available to the authors. However, due to the bandwidth of employed UV optical filter, this does not incur significant performance degradation. Communication performance enhancement can be expected if the optical filter wavelength can match the UV laser

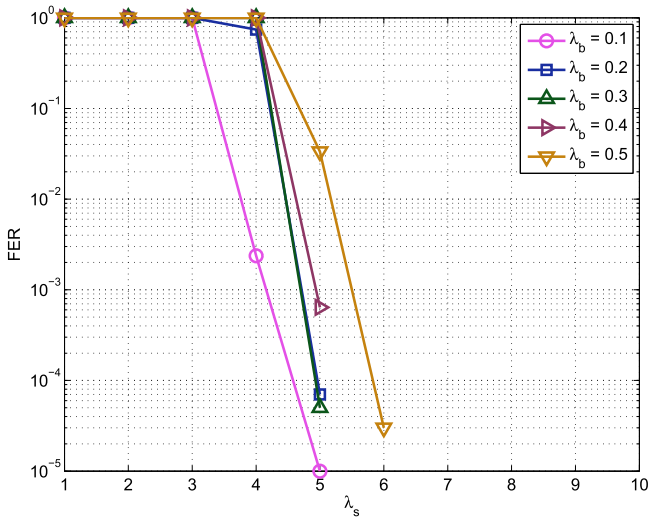

Fig. 6. The FER against λ_s for different λ_b.

TABLE 2
Specification of Experimental Equipments and Devices

UV laser	Wavelength	266nm
	Electric power	30mW
	Polarization ratio	$> 100:1$ vertical
	Bean divergence (full angle)	< 0.8mrad
	Beam diameter (at exit)	0.6 ± 0.12mm
	Aperture size	300mm $\times$ 280mm $\times$ 91mm
Driver of modulator	Supply voltage	$+12$V
	Supply current	≤ 3A
	RF Power Output	10W
	Aperture size	95mm $\times$ 70mm $\times$ 25.2mm
AO modulator	Wavelength	From 193nm to 266nm
	Transmission	$> 99.6\%$
	Frequency	110MHz
	Diffraction efficiency	$\geq 70\%$
	Optical polarisation	Linear
	Aperture size	77mm $\times$ 63.5mm $\times$ 40.2mm
UV optical filter	Peak wavelength	264nm
	Peak transmission	28.2%
	Full width at half maximum	20nm
	Aperture size	Φ31.5mm $\times$28.3mm
PMT	Spectral response	From 160nm to 320nm
	Quantum efficiency	Around 30% at 264nm
	Dark counts	< 10 per second
	Anode pulse rise time	2.2ns
	Detection bandwidth	> 200MHz
	Aperture size	Φ32.2mm $\times$94mm

wavelength. The entire experimental system is shown in Fig. 2. Limited by the laboratory space, two OD3 UV optical decay plates are employed to emulate the weak link gain of the scattering channel, where the attenuation factor for each one is 3.4×10^3 and thus the entire path loss is over 1.16×10^7. The sampling rate of ADC module is 100 MHz, and the air-face transmission symbol rate is 2 Mbps.

Fig. 7 plots the output waveform of a PMT under constant UV light power and OOK-modulated signals. Each negative pulse corresponds to one or several detected photoelectrons, where the pulse duration is 10 ns. The distributions on the number of pulses for OOK symbol on and background

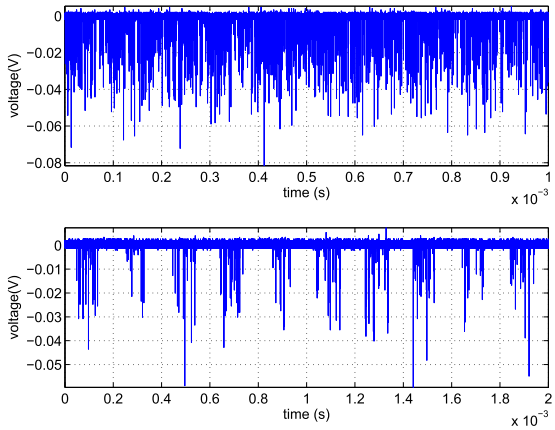

Fig. 7. The output waveform of a PMT with detection of constant signal (top) and OOK-modulated signal (bottom).

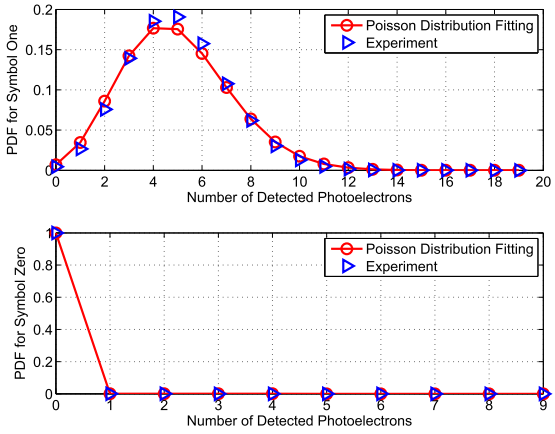

Fig. 8. The distribution on the number of detected photoelectrons for OOK Symbol One (top) and Zero (bottom).

TABLE 3
Parameters and Results of Outdoor Field Test

Parameters	Value
Transmission Power	120mW
Transmission Range	1.03km
Scattering Angle	$\approx 1^\circ$
UV Light Wavelength	266nm
Air-face Symbol Rate	2Mbps
Total Number of Frames	1.7×10^4
Number of Miss Synchronization	221
Number of Error Frames	5

radiation are illustrated in Fig. 8, where Poisson distribution fitting is also plotted for comparison. We have also conducted real-time communication for lab test and obtained the following results. For totally 2×10^4 transmitted frames, miss synchronization occurs for fewer than 50 frames, and decoding error occurs for only 1 frame. Based on above test results, we conclude that the throughput is nearly $\left[1 - (50 + 1)/(2 \times 10^4)\right] \times 1263/(1263 + 17 + 64) \times 0.6 \times 2$ Mbps ≈ 1.125 Mbps.

Fig. 9. The location of transmitter and receiver.

Fig. 10. The transmitter-side test bed.

4.3 Field Test over 1 km

We carried out the outdoor field test on the real-time UV communication. The locations of transmitter and receivers were placed in two buildings shown in Fig. 9. The transmission distance was 1.03 kilometers and about 1 degree offset angle was adopted. The date of outdoor field test was Apr. 21st in 2017, where the weather conditions were 11 $^{\circ}$C$-$22 $^{\circ}$C, cloudy, and northwest wind of 5.5 $\sim$ 7.9 m/s. All parameters for outdoor field test are shown in Table 3. We show the transmitter-side and receiver-side test bed in Figs. 10 and 11, respectively.

The results of field test are shown in Table 3. For totally 1.7×10^4 transmitted frames, miss synchronization occurs for 221 frames, and decoding error occurs for only 5 frames. Hence the

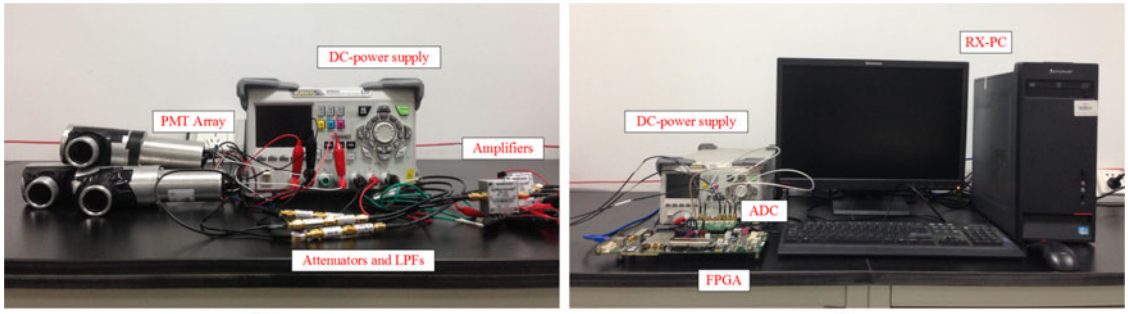

Fig. 11. The receiver-side test bed.

results imply that the throughput is nearly $\left[1-(221+5)/(1.7\times10^4)\right]\times1263/(1263+17+64)\times0.6\times2$ Mbps ≈ 1.113 Mbps.

5. Conclusion

We have designed the system and finished hardware realization based on receiver diversity for the NLOS UV scattering communication over 1 km, where the system throughput can reach 1 Mbps. Higher data rate and longer transmission range can be achieved if more powerful optical devices and more capacity approaching coded modulation are employed, which remains for future work.

References

[1] G. A. Shaw, A. M. Siegel, and J. Model, "Extending the range and performance of non-line-of-sight ultraviolet communication links," in *Proc. Defense Sec. Symp. Int. Soc Opt. Photon.*, Orlando, Florida, USA, Apr. 17, 2006.
[2] Z. Xu and B. M. Sadler, "Ultraviolet communications: Potential and state-of-the-art," *IEEE Commun. Mag.*, vol. 46, no. 5, pp. 67–73, May 2008.
[3] W. Lin *et al.*, "10 m/500 Mbps WDM visible light communication systems," *Opt. Exp.*, vol. 20, no. 9, pp. 9919–9924, 2012.
[4] C. H. Yeh, L. Y. Wei, and C. W. Chow, "Using a single VCSEL source employing OFDM downstream signal and remodulated OOK upstream signal for bi-directional visible light communications," *Sci. Rep.*, vol. 7, no. 1, 2017, Art no. 15846.
[5] W. C. Wang, C. W. Chow, L. Y. Wei, Y. Liu, and C. H. Yeh, "Long distance non-line-of-sight (NLOS) visible light signal detection based on rolling-shutter-patterning of mobile-phone camera," *Opt. Exp.*, vol. 25, no. 9, pp. 10103–10108, 2017.
[6] J. Sung, C. W. Chow, and C. H. Yeh, "Is blue optical filter necessary in high speed phosphor-based white light LED visible light communications?" *Opt. Exp.*, vol. 22, no. 17, pp. 20646–20651, 2014.
[7] M. R. Frey, "Information capacity of the Poisson channel," *IEEE Trans. Inf. Theory*, vol. 37, no. 2, pp. 244–256, Mar. 1991.
[8] A. D. Wyner, "Capacity and error exponent for the direct detection photon channel — Part I–II," *IEEE Trans. Inf. Theory*, vol. 34, no. 6, pp. 1449–1471, Nov. 1988.
[9] J. Cao, S. Hranilovic, and J. Chen, "Capacity-achieving distributions for the discrete-time Poisson channel — Part I–II," *IEEE Trans. Commun.*, vol. 62, no. 1, pp. 194–213, Jan. 2014.
[10] A. Lapidoth and S. M. Moser, "On the capacity of the discrete-time Poisson channel," *IEEE Trans. Inf. Theory*, vol. 55, no. 1, pp. 303–322, Jan. 2009.
[11] S. M. Haas and J. H. Shapiro, "Capacity of wireless optical communications," *IEEE J. Sel. Areas Commun.*, vol. 55, no. 1, pp. 303–322, Jan. 2009.
[12] K. Chakraborty, S Dey, and M. Franceschetti, "Outage capacity of MIMO Poisson fading channels," *IEEE Trans. Inf. Theory*, vol. 54, no. 11, pp. 4887–4907, Nov. 2008.
[13] H. Ding, G. Chen, A. K. Majumdar, B. M Sadler, and Z. Xu, "Modeling of non-line-of-sight ultraviolet scattering channels for communication," *IEEE J. Sel. Areas Commun.*, vol. 27, no. 9, pp. 1535–1544, Dec. 2009.
[14] H. Zhang, H. Yin, H. Jia, S. Chang, and J. Yang, "Characteristics of non-line-of-sight polarization ultraviolet communication channels," *Appl. Opt.*, vol. 51, no. 35, pp. 8836–8372, Dec. 2012.
[15] Y. Sun and Y. Zhan, "Closed-form impulse response model of non-line-of-sight single-scatter propagation," *J. Opt. Soc. Amer. A*, vol. 33, no. 4, pp. 752–757, Apr. 2016.
[16] R. Drost, T. Moore, and B. Sadler, "Ultraviolet scattering propagation modeling: Analysis of path loss versus range," *J. Opt. Soc. Amer. A*, vol. 30, no. 11, pp. 2259–2265, Nov. 2013.

[17] H. Xiao, Y. Zuo, J. Wu, H. Guo, and J. Lin, "Non-line-of-sight ultraviolet single-scatter propagation model," *Opt. Exp.*, vol. 19, no. 18, pp. 17864–17875, Aug. 2011.
[18] Y. Zuo, H. Xiao, J. Wu, Y. Li, and J. Lin, "Closed-form path loss model of non-line-of-sight ultraviolet single-scatter propagation," *Opt. Lett.*, vol. 38, no. 12, pp. 2116–2118, Jun. 2013.
[19] Q. He, Z. Xu, and B. M. Sadler, "Performance of non-line-of-signt LED based ultraviolet communication receivers," *Opt. Exp.*, vol. 18, no. 12, pp. 12 226–12 238, May 2010.
[20] N. Chatzidiamantis, G. K. Karagiannidis, and M. Uysal, "Generailized maximum-likelihood sequence detection for photon-counting free space optical systems," *IEEE Trans. Commun.*, vol. 58, no. 12, pp. 3381–3385, Dec. 2010.
[21] C. Gong and Z. Xu, "LMMSE SIMO receiver for short-range non-line-of-sight scatterign communication," *IEEE Trans. Wireless Commun.*, vol. 14, no. 10, pp. 5338–5349, Oct. 2015.
[22] M. El-Shimy and S. Hranilovic, "Spatial-diversity imaging receivers for non-line-of-sight solar-blind UV communications," *IEEE/OSA J. Lightw. Technol.*, vol. 33, no. 11, pp. 2246–2255, Jun. 2015.
[23] L. Liao, Z. Li, T. Lang, and G. Chen, "UV LED array based NLOS UV turbulence channel modeling and experimental verification," *Opt. Exp.*, vol. 23, no. 17, pp. 21 825–21 835, Aug. 2015.
[24] K. Wang, C. Gong, D. Zou, and Z. Xu, "Turbulence channel modeling and non-parametric estimation for optical wireless scattering communication," *IEEE/OSA J. Lightw. Technol.*, vol. 35, no. 13, pp. 2746–2756, Apr. 2017.
[25] G. A. Shaw, A. M. Siegel, J. Model, and A. Geboff, "Deep UV photon-counting detectors and applications," *SPIE Defense, Sec., Sens. Int. Soc. Opt. Photon.*, Orlando, Florida, USA, Apr. 13, 2009.
[26] G. Chen, L. Liao, Z. Li, R. J. Drost, and B. M. Sadler, "Experimental and simulated evaluation of long distance NLOS UV communication," *in Proc. IEEE 9th Int. Symp. Commun. Syst., Netw. Digit. Signal Process.,* Manchester, UK, Jul. 23–25, 2014, pp. 904–909.
[27] A. M. Siegel, G. A. Shaw, and J. Model, "Short-range communication with ultraviolet LEDs," in *Proc. Opt. Sci. Technol. SPIE 49th Annu. Meeting Int. Soc. Opt. Photon.*, Denver, CO, USA, Aug. 2, 2004.
[28] D. Han, Y. Liu, K. Zhang, P. Luo, and M. Zhang, "Theoretical and experimental research on diversity reception technology in NLOS UV communication system," *Opt. Exp.*, vol. 20, no. 14, pp. 15833–15842, Jun. 2012.
[29] M. Wu, D. Han, X. Zhang, F. Zhang, M. Zhang, and G. Yue, "Experimental research and comparison of LDPC and RS channel coding in ultraviolet communication systems," *Opt. Exp.*, vol. 22, no. 5, pp. 5422–5430, Feb. 2014.
[30] L. Guo, D. Meng, K. Liu, X. Mu, W. Feng, and D. Han, "Experimental research on the MRC diversity reception algorithm for UV communication," *Appl. Opt.*, vol. 54, no. 16, pp. 5050–5056, Jun. 2015.
[31] H. Qin, Y. Zuo, D. Zhang, Y. Li, and J. Wu, "Received response based heuristic LDPC code for short-range non-line-of-sight ultraviolet communication," *Opt. Exp.*, vol. 25, no. 5, pp. 5018–5030, Mar. 2017.
[32] K. Wang, C. Gong, D. Zou, X. Jin, and Z. Xu, "Demonstration of a 400 kbps real-time non-line-of-sight laser-based ultraviolet communication system over 500 m," *Chin. Opt. Lett.*, vol. 15, no. 4, p. 040602, Apr. 2017.
[33] X. Liu, C. Gong, S. Li, and Z. Xu, "Signal characterization and receiver design for visible light communication under weak illuminance," *IEEE Commun. Lett.*, vol. 20, no. 7, pp. 1349–1352, Jul. 2016.
[34] M. Yang, W. E. Ryan, and Y. Li, "Design of efficiently encodable moderate-length high-rate irregular LDPC codes," *IEEE Trans. Commun.*, vol. 52, no. 4, pp. 564–571, Apr. 2004.
[35] M. P. C. Fossorier, "Quasicyclic low-density parity-check codes from circulant permutation matrices," *IEEE Trans. Inf. Theory*, vol. 50, no. 8, pp. 1788–1793, Aug. 2004.
[36] J. Chen, A. Dholakia, E. Eleftheriou, M. P. C. Fossorier, and X. Y. Hu, "Reduced-complexity decoding of LDPC codes," *IEEE Trans. Commun.*, vol. 53, no. 8, pp. 1288–1299, Aug. 2005.